IEEE Access
Multidisciplinary ⋮ Rapid Review ⋮ Open Access Journal

Received 14 November 2022, accepted 29 November 2022, date of publication 1 December 2022,
date of current version 6 December 2022.

Digital Object Identifier 10.1109/ACCESS.2022.3226335

RESEARCH ARTICLE

High-Efficiency Drive Method of Adjustable Field IPMSM Utilizing Magnetic Saturation

KIYOHIRO IWAMA, (Graduate Student Member, IEEE),
AND TOSHIHIKO NOGUCHI, (Senior Member, IEEE)
Department of Environment and Energy Systems, Graduate School of Science and Technology, Shizuoka University, Hamamatsu 432-8561, Japan
Corresponding author: Kiyohiro Iwama (iwama.kiyohiro.14@shizuoka.ac.jp)

This work was supported by JSPS KAKENHI under Grant JP21K04022.

ABSTRACT This paper describes a high-efficiency drive method of an adjustable field Interior Permanent Magnet Synchronous Motor (IPMSM) utilizing magnetic saturation. The adjustable field IPMSM can control the magnetic field flux using magnetic saturation caused by a modulation current. In general, it is said that motor efficiency is high at operating points where the copper loss and the iron loss are balanced. However, the high-efficiency drive range of a conventional PMSM is narrow because the magnetic field of the PMSM is constant. On the other hand, it is possible in the proposed adjustable field IPMSM to expand the high-efficiency drive range because the field amount can freely be adjusted by the modulation current. Therefore, this paper examines an optimal modulation current for a high-efficiency operation. To derive the optimal modulation current, losses and efficiency of the proposed adjustable field IPMSM are formulated based on the measured motor parameters. In addition, it is confirmed from several experimental tests that the high-efficiency driving range can be expanded due to the optimal modulation current.

INDEX TERMS Adjustable field, PMSM, magnetic saturation, motor efficiency, copper loss, iron loss.

I. INTRODUCTION

In recent years, adjustable field PMSMs have been widely researched for driving range expansion [1], [2], [3], [4], [5], [6], [7], [8], [9], [10], [11], [12]. The authors also have studied the adjustable field IPMSM focusing on the magnetic saturation of a soft magnetic material [13] and [14]. We call the motor the adjustable field IPMSM based on permeability modulation because the motor can control the magnetic field while modulating the permeability of the magnetic leakage paths between PMs. In the reference [13], it could be confirmed that the prototype of the adjustable field IPMSM based on permeability modulation can expand the driving range utilizing magnetic field control. In the reference [14], a three-phase four-wire inverter was introduced as a drive circuit for the prototype motor. The three-phase four-wire inverter can supply a square wave zero-sequence current to the prototype in addition to the d-axis current i_d and the q-axis current i_q. As a result, it has been revealed that the proposed drive circuit is more straightforward and efficient in terms of system volume and switching loss than the conventional adjustable field PMSM drive system. In addition, the reference [13] and [14] revealed that the proposed adjustable field method could achieve field control with lower copper loss and harmonics than the conventional field weakening control [15], [16], [17], [18], [19].

In contrast to these references [13] and [14], this paper examines a new added value of adjustable field IPMSM, which is to expand the high-efficiency driving range. Fig. 1 shows the relationships between the rotating speed and the torque (NT characteristics) of a general PMSM and the efficiency maps within its driving range. Fig. 1(a) and Fig. 1(b) are NT characteristics and efficiency maps of PMSM with a high magnetic field Ψ_f and PMSM with a low Ψ_f, respectively. Comparing the efficiencies in the driving range common to the NT characteristics of both PMSMs, the PMSM with the high Ψ_f can achieve a high-efficiency drive at the high torque operating point because the armature current to deliver the high torque can be reduced. In contrast, since the significant loss at the low-toque-high-speed operating point

The associate editor coordinating the review of this manuscript and approving it for publication was Zhong Wu.

is iron loss, not copper loss, the efficiency at the low-torque-high-speed operating point can be improved by designing the Ψ_f to be small, as shown in Fig. 1(b).

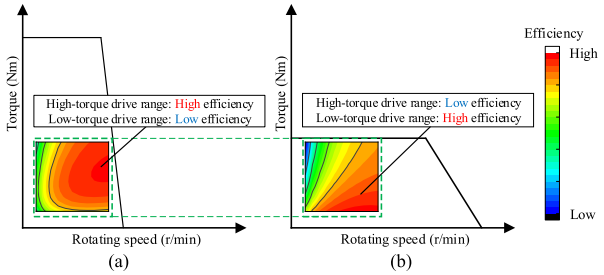

FIGURE 1. NT characteristics and efficiency maps. (a) PMSM with high magnetic field. (b) PMSM with low magnetic field.

TABLE 1. Evaluations of magnetic field controllability.

Adjustable field PMSM	Reference	Continuity	Independence
Memory motor	[1]-[5]	Not good	Good
Variable leakage flux motor	[6]-[8]	Good	Not good
MATRIX motor	[9], [10]	Not good	Good
Hybrid motor	[11], [12]	Good	Good
Proposed adjustable field IPMSM	[13], [14]	Good	Good

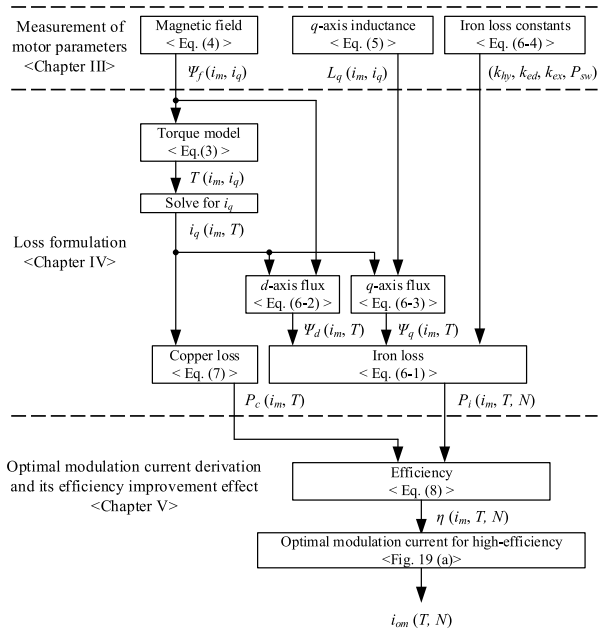

FIGURE 2. Flowchart of proposed high-efficiency drive method.

On the other hand, adjustable field PMSM that can freely adjust the Ψ_f can be expected to expand the high-efficiency driving range by decreasing the Ψ_f in the low-torque operating point and increasing the Ψ_f in the high-torque operating point.

In order to accurately control the Ψ_f according to an arbitrary operating point, the continuity and independence of the Ψ_f control are required. TABLE 1 shows the evaluations of continuity and independence in adjustable field methods. Memory motor introduced in the references [1], [2], [3], [4], [5] can widely control the Ψ_f utilizing re- and de-magnetization of the PM. However, the magnetic flux generated from the PM changes drastically at the PM operating point near the knick point due to temperature and external magnetic field, so it is difficult to control the Ψ_f continuously and accurately. Variable leakage flux motor proposed in the references [6], [7], [8] can achieve an expansive driving range by controlling the amount of magnetic flux leaking on the rotor using a q-axis armature reaction. However, when an arbitrary PM torque is delivered, the i_q is uniquely determined, so the independence of the Ψ_f control is not good. MATRIX motor described in the reference [9] and [10] has six winding per electrical period and can change the vector length of interlinkage flux by switching over the winding configuration (e.g., six-phase or three-phase). However, due to the principle that the winding structure is changed over, it is impossible to control the Ψ_f continuously.

On the other hand, hybrid motor reported in the reference [11] and [12] can continuously control the Ψ_f independently of the armature current by using field current for Ψ_f control. Similarly, the adjustable field IPMSM based on permeability modulation that the authors introduced in the reference [13] and [14] can also accurately adjust the Ψ_f depending on the modulation current i_m. In other words, the hybrid motor and the proposed motor can be expected to expand the high-efficiency range by adjusting the Ψ_f according to an arbitrary operating point.

Therefore, this paper examines a method for deriving the optimal modulation current i_{om} that maximizes efficiency at any operating point through the finite element analysis (FEA) and experimental tests with the prototype of the proposed adjustable field IPMSM based on permeability modulation. As a result, FEA simulations and experimental tests confirm the following contributions of this paper:

(1) The efficiency of the adjustable field IPMSM can be predicted with high accuracy by measuring the motor parameters of the Ψ_f, q-axis inductance, and no-load loss without considering complex motor geometry and material properties;
(2) In the high-torque driving range, copper and iron loss can be reduced by effectively using the adjustable field control. In particular, for iron loss, the more the rotating speed increases, the more valuable the adjustable field control becomes;
(3) By controlling the optimal Ψ_f, a maximum of around 4 % improves the efficiency compared to the case where the adjustable field control is not used like a normal PMSM.

This paper is organized as follows: Chapter II explains the prototype's specifications. Chapters III to V present a theoretical explanation of the proposed high-efficiency drive method based on Fig. 2. The prototype motor parameters, such as Ψ_f, q-axis inductance L_q, and iron loss constants,

are measured in Chapter III. In Chapter IV, the losses are formulated based on the measured parameters, and the i_{om} is calculated using the loss formulas in Chapter V. Finally, the prototype's efficiency is measured, and it is concluded that the high-efficiency driving range can be expanded due to the i_{om}.

II. SPECIFICATIONS OF PROTOTYPE MOTOR

Fig. 3 and TABLE 2 show the prototype motor model and its specifications, respectively. The stator and rotor cores are split into two parts, and the modulation winding is inserted between two stator cores. In addition, as shown in TABLE 2, the current densities of the two windings, the armature and the modulation winding, are designed to be around 13 Arms/mm^2. At the maximum current density, the q-axis current of 70 A and the i_m of 6.6 A are supplied to the armature and the modulation winding, respectively. The modulation flux that penetrates to a 3-dimensional (3D) magnetic path, including the stator frame and the rotor shaft, can be generated by supplying the i_m to the modulation winding. Therefore, the stator frame and the rotor shaft consist of SS400 and SUS403, respectively, which are soft magnetic materials. The prototype motor can control the Ψ_f by using the modulation flux and modulating the permeability of the magnetic leakage paths shown in Fig. 4.

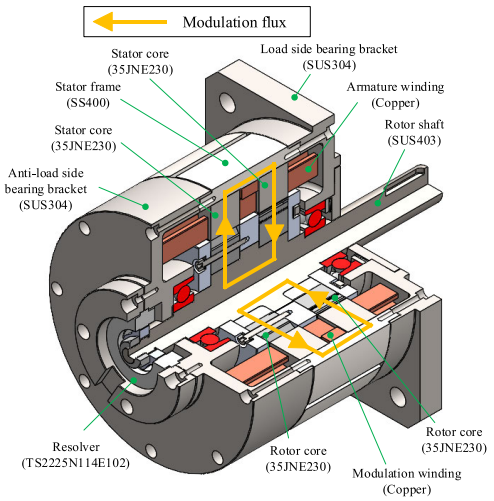

FIGURE 3. Development view of prototype motor.

TABLE 2. Specifications of prototype motor.

Parameter	Symbol	Value
Number of pole pairs	P_n	4 pole pairs
Number of slots	-	48 slots
Number of armature winding turns	-	6 turns/slot
Number of modulation winding turns	-	140 turns
Max. current density of armature winding	-	13.0 A_{rms}/ mm^2
Max. current density of modulation winding	-	13.1 A_{rms}/ mm^2
Resistance of armature winding	R_a	0.0851 Ω
Resistance of modulation winding	R_m	2.10 Ω
Stator diameter	-	ϕ 148 mm
Rotor diameter	-	ϕ 96.6 mm
Air gap length	-	0.5 mm
Core stack length	-	48 mm

The basic principle of the proposed adjustable field method utilizing magnetic saturation is explained using a simplified model shown in Fig.5. Fig. 5(a) shows the vector of modulation flux. The modulation flux is generated by the modulation winding and penetrates in a radial direction on the rotor core. Fig. 5(b) shows the PM flux when the modulation current i_m is not given to the modulation winding. The prototype motor has the magnetic leakage paths as shown in Fig. 4, so much PM flux leaks on the rotor. In other words, the Ψ_f is low in this condition. Fig. 5(c) shows the magnetic flux vector when the i_m is supplied. The magnetic leakage path pointed by the blue line is likely to be magnetically saturated because the directions of the two fluxes are aligned. In this condition, as shown in Fig. 5(c), due to the magnetic saturation of the one-side magnetic leakage path, the PM flux short-circuited in the rotor decreases, so the Ψ_f increases. As the i_m further increases, the modulation flux becomes the bias flux of the one-side magnetic pole, as shown in Fig. 5(d). Therefore, the Ψ_f further increases. As shown in Fig. 5(d), the magnetic field of the proposed adjustable field IPMSM reaches its limit, when the leakage paths on both sides are magnetically saturated. Fig. 6 shows the photograph of the prototype motor. The stator cores are shrink-fitted to the stator frame to reduce the air gap in the 3D magnetic path.

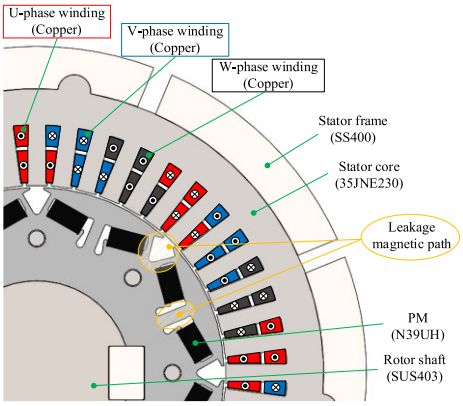

FIGURE 4. Cross section of prototype motor.

III. MEASUREMENT OF MOTOR PARAMETERS

A. EXPERIMENTAL SETUP

Fig. 7 shows the experimental setup in this paper. Fig. 7(a) shows the measuring instruments and the prototype motor's drive system. The motor input power is measured by the power meter WT1800E, made by Yokogawa Test & Measurement Corporation. It is necessary for the proposed adjustable fied IPMSM to supply the i_m in addition to the armature current. In this paper, voltage source three-phase inverter MWINV-2022B, Myway Plus Corporation, provides the armature current. Since the rated capacity of MWINV-2022B is 20.2 kVA and the maximum output of the prototype in this paper is around 3 kW, the output capacity of the inverter has a sufficient margin. In addition, to supply the maximum current density of the armature winding, it is necessary to provide

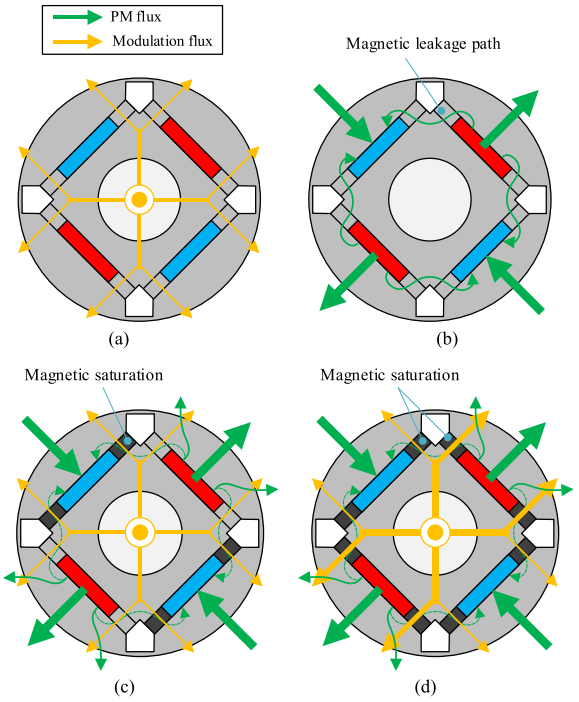

FIGURE 5. Basic principle of proposed adjustable field method utilizing magnetic saturation. (a) Modulation flux. (b) PM flux. (c) Magnetic flux vectors when one-side magnetic leakage path is magnetically saturated. (d) Magnetic flux vectors when magnetic leakage paths on both sides are magnetically saturated.

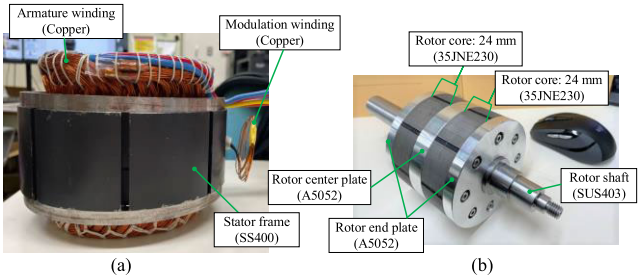

FIGURE 6. Photograph of prototype motor. (a) Stator. (b) Rotor.

a line current of 40 A_{rms} from the inverter. However, since the inverter's rated current is about 58.4 A_{rms}, there is also a margin in the output current capacity. On the other hand, the i_m is supplied by DC power supply ZX-800L, TAKASAGO, LTD. The torque is measured by torque meter UTMIII-50Nm, the product of Unipluse Corporation, as shown in Fig. 7(b).

B. RELATIONSHIP BETWEEN MAGNETIC FIELD AND CURRENTS

In this chapter, the prototype motor parameters are measured. The Ψ_f and the L_q are calculated based on a voltage equation of the prototype. The voltage equation is expressed as follows:

$$\begin{bmatrix} v_d \\ v_q \end{bmatrix} = \begin{bmatrix} R_a + \mathrm{p}L_d\left(i_m, i_d, i_q\right) & -\omega L_q\left(i_m, i_d, i_q\right) \\ \omega L_d\left(i_m, i_d, i_q\right) & R_a + \mathrm{p}L_q\left(i_m, i_d, i_q\right) \end{bmatrix} \begin{bmatrix} i_d \\ i_q \end{bmatrix} + \begin{bmatrix} 0 \\ \omega\Psi_f\left(i_m, i_d, i_q\right) \end{bmatrix} \quad (1)$$

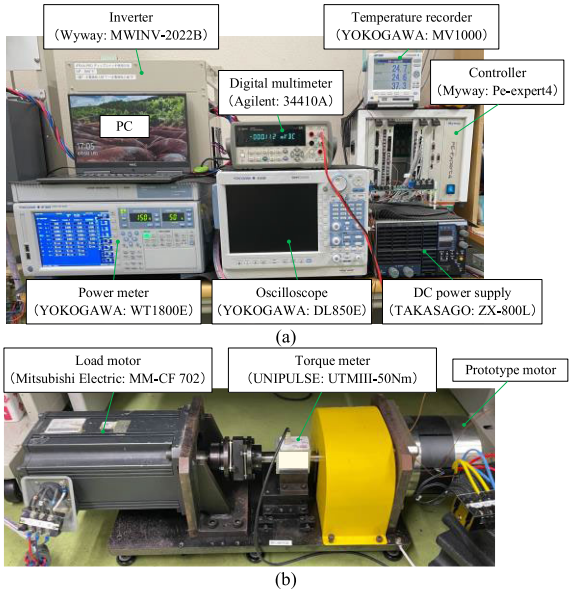

FIGURE 7. Experimental setup. (a) Measuring instruments and drive system for prototype motor. (b) Motor test rig.

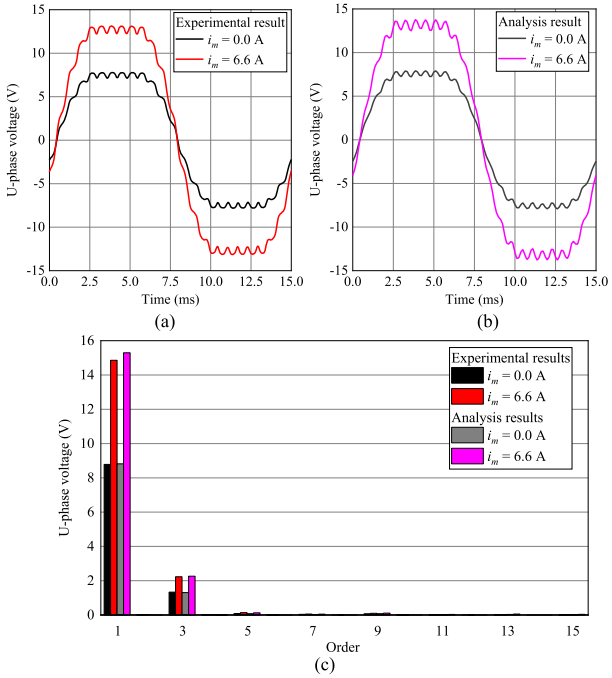

FIGURE 8. U-phase voltage in no-load condition at rotating speed of 1000 r/min. (a) Experimental resuts. (b) Analysis results. (b) FFT results.

where v_d and v_q are the voltages on the dq reference frame, L_d is the d-axis inductance, ω is an electrical angular speed, and p is a differential operator. As can be seen in (1), the inductances (L_d and L_q) and the magnetic field Ψ_f are functions of currents because these are affected by magnetic saturation and PM demagnetization depending on current values. The goal of this chapter is to reveal the current dependence of the parameters. However, since there are three unknown parameters, $L_d(i_m, i_d, i_q)$, $L_q(i_m, i_d, i_q)$, and $\Psi_f\ (i_m, i_d, i_q)$, the

two simultaneous equations expressed in (1) are insufficient. Therefore, this paper adds the condition that $i_d = 0$ for simplicity. Under this condition, the motor parameters are calculated by using the following equations:

$$\begin{cases} \Psi_f\left(i_m, i_q\right) = \dfrac{v_q - R_a i_q}{\omega} & (2-1) \\ L_q\left(i_m, i_q\right) = -\dfrac{v_d}{\omega i_q}. & (2-2) \end{cases}$$

First, the i_m dependence of the Ψ_f (i_m, i_q) is examined. Fig. 8 shows the waveforms of U-phase voltage in no-load conditions and its FFT result. However, the rotating speed N is controlled at 1000 r/min by the load motor. It can be confirmed from this figure that the fundamental component of the U-phase voltage increases by 69.2 % by supplying the i_m of 6.6 A. According to this result, it can be said that the Ψ_f of the prototype motor depends on the i_m. In addition, the analysis result is added to the same figure as the experimental result. However, all analysis results in this paper are obtained by FEA software JMAG-Designer 21.0. As shown in this figure, the observed value is slightly smaller by 2.9 % than the analysis value, but the testing results are in good agreement with the analysis results. It is thought that the experimental value is slightly smaller because of manufacturing errors such as air gap length and magnetic leakage path width. Fig. 9 shows the relationship between the Ψ_f and the i_m without the i_q. As shown in Fig. 9, the larger the i_m, the larger the Ψ_f. The experimental values of Ψ_f (0.0,0) and Ψ_f (6.6,0) are 25.7 mWb and 43.4 mWb, respectively.

Next, the i_q dependence of the Ψ_f (i_m, i_q) is investigated. Fig. 10 shows the experimental and analysis results of the relationship between the i_q and the torque (IT characteristic). As shown in this figure, the experimental results match the analysis. In addition, the calculation values using Ψ_f (0.0,0) and Ψ_f (6.6,0) are shown by dotted lines in Fig. 10. However, the following equation is used to calculate the torque T:

$$T = P_n \Psi_f i_q. \tag{3}$$

When the i_m is 0.0 A, the effect of the armature reaction increases as the i_q increases, as in variable leakage flux motor presented in the reference [6], [7], [8], and the Ψ_f also increases. On the other hand, when the i_m is 6.6 A, the Ψ_f slightly reduces as the i_q increases because of magnetic saturation in the stator teeth due to the modulation flux. In other words, not only the i_m but also the i_q is the independent variable of the Ψ_f.

Fig. 11 shows the measured values of the $\Psi_f(i_m, i_q)$. In addition, approximated values obtained using the least-squares method based on the experimental values are shown in the same figure. However, the approximate formula is expressed as

$$\begin{aligned} \Psi_f\left(i_m, i_q\right) = &\left(m_{42} i_m^4 + m_{22} i_m^2 + m_{02}\right) i_q^2 \\ &+ \left(m_{41} i_m^4 + m_{21} i_m^2 + m_{01}\right) i_q \\ &+ \left(m_{40} i_m^4 + m_{20} i_m^2 + m_{00}\right) \end{aligned} \tag{4-1}$$

where the constants are set as follows:

$$\begin{cases} \left(m_{42}, m_{22}, m_{02}\right) = \left(1.21\times10^{-9}, -1.02\times10^{-7}, 8.56\times10^{-7}\right) \\ \left(m_{41}, m_{21}, m_{01}\right) = \left(-2.17\times10^{-8}, 7.77\times10^{-7}, 5.78\times10^{-5}\right) \\ \left(m_{40}, m_{20}, m_{00}\right) = \left(-4.96\times10^{-6}, 6.55\times10^{-4}, 2.44\times10^{-2}\right). \end{cases} \tag{4-2}$$

To evaluate the accuracy of the approximation, mean absolute percentage error (MAPE) is calculated and added to Fig. 11. In case the MAPE is large, it will adversely affect the efficiency calculation results. However, as shown in Fig. 11, the MAPE is a reasonably small value, so it has little effect on the calculation result of the efficiency. In addition, with regard to the i_m, the Ψ_f depends on the absolute value of the i_m due to the principle of utilizing magnetic saturation, and the i_m appears only in components of even orders.

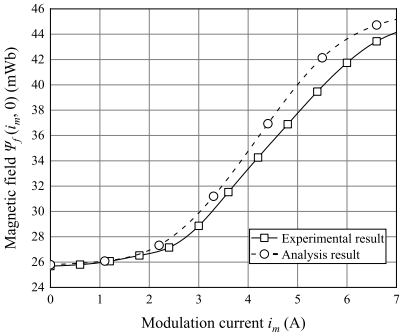

FIGURE 9. Relationship between magnetic field and modulation current without q-axis current.

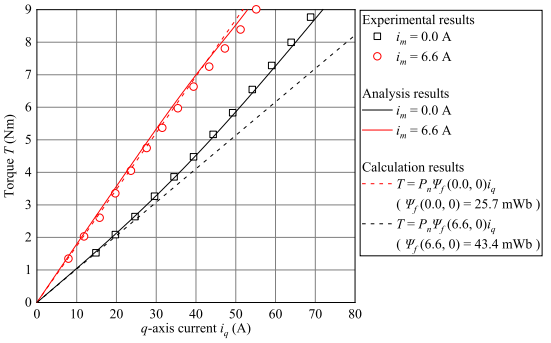

FIGURE 10. Experimental result of IT characteristics.

C. RELATIONSHIP BETWEEN Q-AXIS INDUCTANCE AND CURRENTS

Fig. 12 shows the measured values of the L_q (i_m, i_q). It can be seen from Fig. 12 that the L_q reduces as the i_m or the i_q increase due to magnetic saturation. Therefore, the L_q is also regarded as a function of the currents and approximated as follows:

$$\begin{aligned} L_q\left(i_m, i_q\right) = &\left(l_{42} i_m^4 + l_{22} i_m^2 + l_{02}\right) i_q^2 \\ &+ \left(l_{41} i_m^4 + l_{21} i_m^2 + l_{01}\right) i_q \\ &+ \left(l_{40} i_m^4 + l_{20} i_m^2 + l_{00}\right) \end{aligned} \tag{5-1}$$

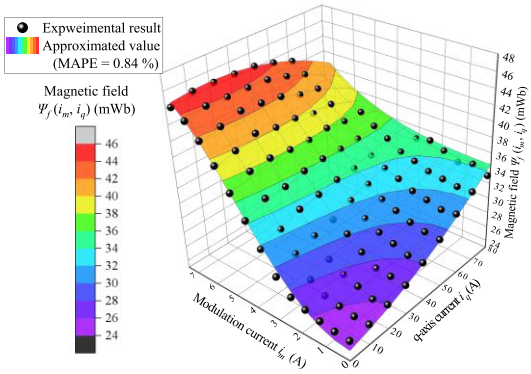

FIGURE 11. Relationship between magnetic field and currents.

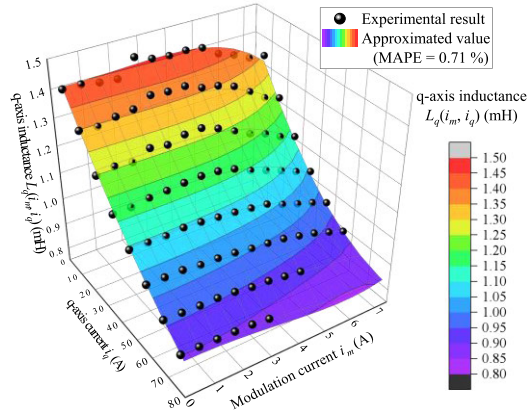

FIGURE 12. Relationship between q-axis inductance and currents.

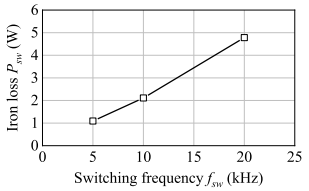

FIGURE 13. Iron loss due to switching.

where the constants are set as follows:

$$\begin{cases} (l_{42}, l_{22}, l_{02}) = \left(2.36\times10^{-11}, -3.23\times10^{-10}, 3.40\times10^{-8}\right) \\ (l_{41}, l_{21}, l_{01}) = \left(-4.27\times10^{-10}, -3.83\times10^{-8}, -1.10\times10^{-5}\right) \\ (l_{40}, l_{20}, l_{00}) = \left(-7.11\times10^{-8}, 2.03\times10^{-6}, 1.55\times10^{-3}\right). \end{cases} \quad (5-2)$$

As well as the Ψ_f approximation, the accuracy of the L_q approximation is evaluated by MAPE. As shown in Fig. 12, it can be seen the MAPE is very small, even in the approximation of the L_q.

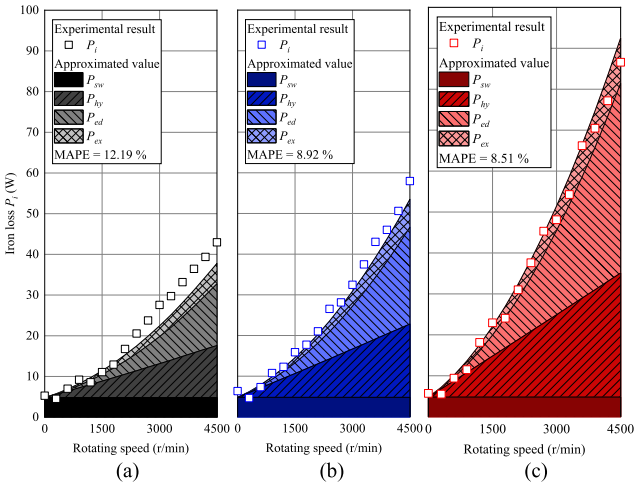

FIGURE 14. Measurement results of no-load loss. (a) i_m = 0.0 A. (b) i_m = 3.3 A. (c) i_m = 6.6 A.

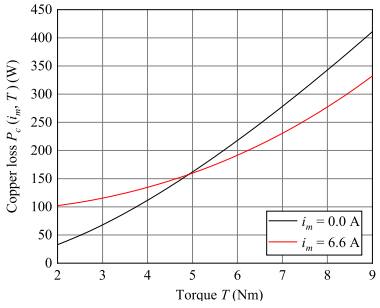

FIGURE 15. Calculation result of copper loss.

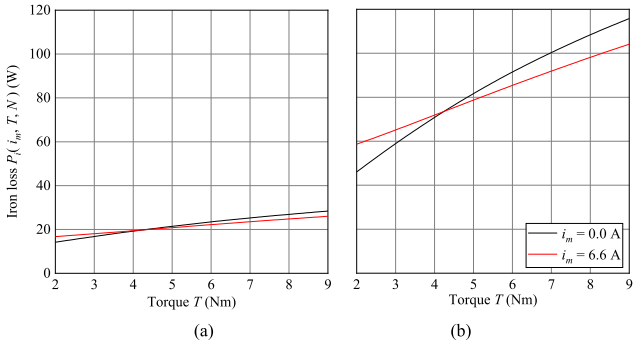

FIGURE 16. Calculation result of iron loss. (a) N = 1000 r/min. (b) N = 3000 r/min.

D. IRON LOSS CONSTANTS

The iron loss P_i of the prototype motor is expressed as follows based on the references [20], [21], [23]:

$$\begin{aligned} P_i\left(i_m, i_q, N\right) &= P_{hy} + P_{ed} + P_{ex} + P_{sw} \\ &= k_{hy}\left(\Psi_d^{1.6} + \Psi_q^{1.6}\right)N + k_{ed}\left(\Psi_d^{2.0} + \Psi_q^{2.0}\right)N^2 \\ &\quad + k_{ex}\left(\Psi_d^{1.5} + \Psi_q^{1.5}\right)N^{1.5} + P_{sw} \end{aligned} \quad (6-1)$$

where Ψ_d and Ψ_q are the d- and q-axis flux, respectively, and these are expressed as

$$\begin{cases} \Psi_d\left(i_m, i_q\right) = \Psi_f\left(i_m, i_q\right) & (6-2) \\ \Psi_q\left(i_m, i_q\right) = L_q\left(i_m, i_q\right) \cdot i_q. & (6-3) \end{cases}$$

In addition, k_{hy}, k_{ed}, and k_{ex} are constants for hysteresis loss P_{hy}, eddy current loss P_{ed}, and excess loss P_{ex}, respectively. These constants are determined by the motor geometry, materials, etc. However, it is difficult to derive the constants accurately based on these motor specifications, so this paper investigates them by measuring the no-load loss. In addition, P_{sw} is the iron loss generated by time harmonics from a voltage source inverter. The time harmonics are caused due to the switching of the inverter, so the P_{sw} is the function of the switching frequency f_{sw}, not the rotating speed N. Fig. 13 shows the relationship between the motor input power and the f_{sw} when the prototype motor disconnects from the load and the N is controlled with the command of 0 r/min. Despite no load and no rotation, there is the input power, which is the iron loss P_{sw} caused by the switching of the inverter. As shown in Fig. 13, the P_{sw} depends on the f_{sw} and increases as the f_{sw} increases. In the following experiments, the f_{sw} is set at 20 kHz, so the P_{sw} is 4.8 W.

Fig. 14 shows the motor input when the prototype motor is controlled at constant speed in no-load conditions. The motor input includes mechanical loss, but the mechanical loss is negligibly small. This figure shows that the P_i increases as the Ψ_f or N increases. The calculation values assuming the iron loss constants as follows are shown in Fig. 14:

$$\left(k_{hy}, k_{ed}, k_{ex}, P_{sw}\right) = \left(1.0, 1.2 \times 10^{-3}, 4.0 \times 10^{-3}, 4.8\right). \quad (6-4)$$

As shown in Fig. 14, the MAPE of the P_i approximation is larger than that of the Ψ_f and L_q because only the magnetic flux of the fundamental component is considered when calculating P_i, as expressed in Eq. (6). However, the MAPE is small, around 10 %, and it can be seen that the approximated values agree well with the experimental values.

IV. LOSS FORMULATION

In this chapter, the losses of the prototype motor are formulated based on the flowchart shown in Fig. 2.

A. COPPER LOSS FORMULATION

The copper loss of the prototype motor is expressed as

$$P_c\left(i_m, i_q\right) = R_m i_m^2 + R_a i_q^2. \quad (7)$$

From (4), it was revealed that the Ψ_f is the function of the i_m and the i_q. In addition, the T can be expressed as (3), so the T can also be described as the function $T\ (i_m, i_q)$ of the currents using (4). Furthermore, by solving the torque equation $T\ (i_m, i_q)$ for the i_q, the i_q required to deliver arbitrary torque T can be derived as $i_q\ (i_m, T)$. Finally, by substituting the $i_q\ (i_m, T)$ into (7), the P_c can be expressed as a function $P_c(i_m, T)$ of the T.

Fig. 15 shows the calculated value of the $P_c(i_m, T)$ when the i_m is 0.0 A or 6.6 A. The black line in this figure is the $P_c(0.0, T)$, which can be regarded as the copper loss of a normal PMSM with a low Ψ_f. On the other hand, the red line is the $P_c(6.6, T)$, and this copper loss includes the additional copper loss that occurs in the modulation winding. From Fig. 15, it can be seen that the $P_c(6.6, T)$ is smaller than the $P_c(0.0, T)$ in the high-torque driving range, even though there is additional copper loss of the modulation winding. For example, when the torque is 9 Nm, the $P_c(6.6, T)$ is 72 W less than $P_c(0.0, T)$. From the above, it can be seen that the copper loss can be suppressed by increasing the i_m in the high-torque driving range and decreasing the i_m in the low-torque driving range.

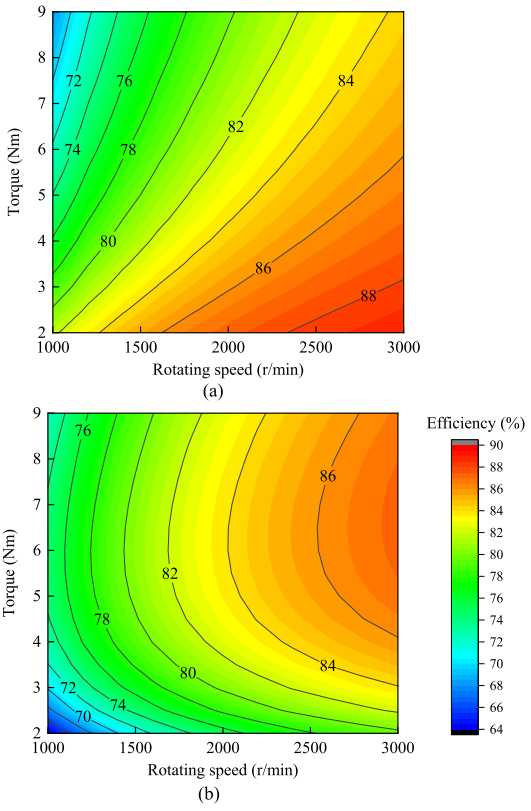

FIGURE 17. Calculation results in efficiency with constant modulation current. (a)η (0.0, T, N). (b) η (6.6, T, N).

B. IRON LOSS FORMULATION

As with the $P_c\ (i_m, T)$, the iron loss $P_i\ (i_m, T, N)$ at any operating point (T, N) can be calculated by substituting the $i_q\ (i_m, T)$ into (6). Fig. 16 shows the calculation result of the $P_i\ (i_m, T, N)$ when the i_m is 0.0 A or 6.6 A. However, the P_i depends on the N, so the P_i is calculated for two rotating speed cases, 1000 r/min and 3000 r/min. This figure shows that regardless of whether the N is 1000 r/min or 3000 r/min, the P_i can be suppressed by increasing the i_m in the high-torque range and decreasing the i_m in the low-torque range. In particular, the higher the N, the more significant P_i

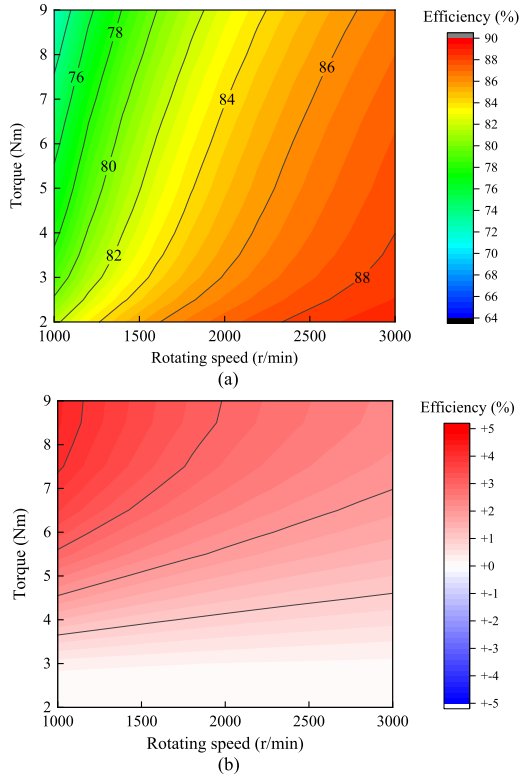

FIGURE 18. Calculation results in efficiency with i_{om}. (a)η (i_{om}, T, N). (b) Difference between η (i_{om}, T, N) and η (0.0, T, N).

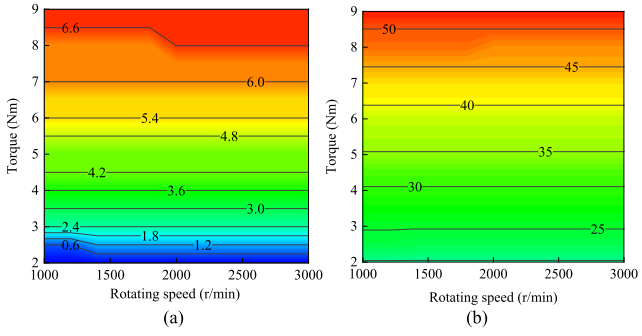

FIGURE 19. Currents for highest efficiency derived by FEA and proposed loss formulation. (a) i_{om}. (b) i_q.

difference. For example, When the N is 3000 r/min, and the T is 9 Nm, the P_i by 12 W can be reduced by giving the i_m of 6.6 A.

V. OPTIMAL MODULATION CURRENT DERIVATION AND ITS EFFICIENCY IMPROVEMENT EFFECT

A. CALCULATION OF EFFICIENCY

In the previous chapter, the copper loss P_c (i_m, T) and the iron loss P_i (i_m, T, N) at arbitrary operating points (T, N) are derived. Therefore, the efficiency map η (i_m, T, N) can be obtained using these loss formulas as follows:

$$\eta\left(i_m, T, N\right) = \frac{\left(2\pi \frac{N}{60}\right) \cdot T}{\left(2\pi \frac{N}{60}\right) \cdot T + \left\{P_c\left(i_m, T\right) + P_i\left(i_m, T, N\right)\right\}}. \tag{8}$$

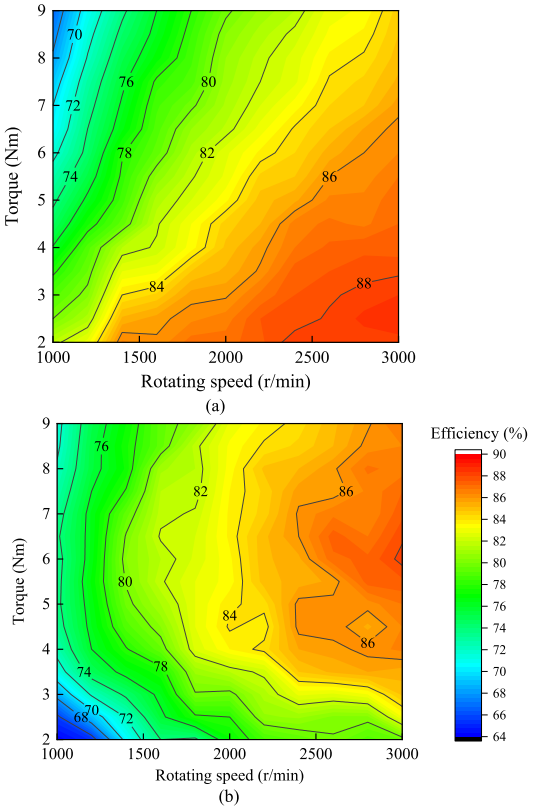

FIGURE 20. Experimental result of efficiency with constant modulation current. (a)η (0.0, T, N). (b) η (6.6, T, N).

Fig. 17 shows η (0.0, T, N) and η (6.6, T, N). Since the i_m is not supplied in the η (0.0, T, N), the η (0.0, T, N) can be considered the same as the efficiency map of a normal IPMSM with a low Ψ_f. On the other hand, the η (6.6, T, N) can be roughly regarded as the efficiency map of a normal PMSM with a large Ψ_f, but there is a difference in that η (6.6, T, N) includes an additional copper loss in the modulation winding. Fig. 17 shows that efficiency can be improved in the high-torque driving range by effectively utilizing the adjustable field function and giving the i_m to strengthen the Ψ_f.

Since the efficiency with any i_m can be obtained as described above, the optimal modulation current i_{om} for the highest efficiency η (i_{om}, T, N) can be calculated. Fig. 18 shows the calculation result of the η (i_{om}, T, N) and the difference between η (i_{om}, T, N) and η (0.0, T, N). However, the current conditions are shown in Fig. 19. As shown in Fig. 18, the efficiency in the high-torque driving range is improved by up to 4 % due to the i_{om}, and it can be expected that the high-efficiency driving range is expanded by supplying the i_{om}. In addition, Fig. 19(a) shows that the i_{om} mainly depends on the output torque.

B. MEASUREMENT OF EFFICIENCY

Finally, the validity of the proposed loss and efficiency equations is examined by comparing the calculation results with the experimental results. Fig. 20 shows the experimental

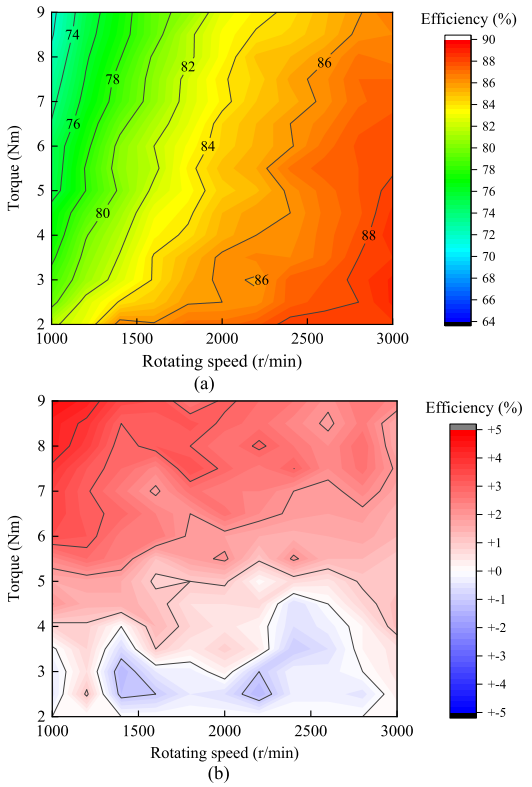

FIGURE 21. Experimental result of efficiency with i_{om}. (a)η (i_{om}, T, N). (b) Difference between η (i_{om}, T, N) and η (0.0, T, N).

results of the efficiency map with the constant i_m of 0.0 A or 6.6 A. As can be seen by comparing this figure with Fig. 17, the calculation results and the measurement results are in good agreement, and it can be said that the proposed loss formulas are valid. In addition, Fig. 21 shows that the high-efficiency driving range can be expanded by using the current conditions shown in Fig. 19. On the other hand, when comparing Fig. 21(b) and Fig. 18(b), it can be seen that there is the error between the calculation and the experimental value in the low-torque driving range. In the low-torque driving range, the main loss factor is iron loss. It was revealed from Fig. 14 that the MAPE of the iron loss approximation is larger than the other approximations described in this paper. For this reason, it is thought that the calculated values of the efficiency map included the error, and there was a difference between the calculated value and the measured value in the low-torque driving range. However, the error is around 1 %, so it can be said that it is pretty tiny.

Based on the above results of the actual machine tests, as shown in Fig. 20, it is confirmed that the efficiency calculation method proposed in this paper can predict the efficiency of the adjustable field IPMSM with high accuracy. In addition, it is revealed in Fig. 21 that the high-efficiency driving range can be expanded by using the optimal modulation current from the proposed efficiency formulation.

VI. CONCLUSION

In this paper, the losses of the adjustable field IPMSM utilizing magnetic saturation were formulated, and the optimal modulation current i_{om} calculation method for the highest efficiency was examined. In addition, several experiments were conducted to confirm the validity of the proposed loss and efficiency formulation. Besides, it was confirmed that the high-efficiency driving range could be expanded using i_{om}. The outline and results of this paper are explained below by chapter.

Chapter I described the characteristics of the conventional adjustable field method and the proposed adjustable field method utilizing magnetic saturation and clarified the prototype's positioning and superiority. The superiorities of the proposed adjustable field method are as follows:

(1) The proposed adjustable field method can continuously control the Ψ_f according to the magnitude of the i_m.
(2) The Ψ_f is independent of drive conditions.

Chapter II presented the principle of the proposed adjustable field method and the design of the prototype. In chapter III, the measurement results were compared with the FEA results. As a comparison result, the difference between the simulation and the experiment is around 3 %, and it was found that the prototype has almost the same characteristics as the FEA model. In addition, in Chapter III, the motor parameters, such as the Ψ_f, the L_q, and the iron loss constants, were measured and approximated by the least-square method. Using MAPE as the approximation evaluation index, we confirmed that the approximation was achieved with high accuracy.

In chapter IV, the losses were formulated based on the measured motor parameters. As a result of the formulation, it was clarified that the effective use of magnetic field control in the prototype produces the following effects.

(1) When the output torque is 9 Nm, the copper loss can be reduced by 72 W by applying the i_m of 6.6 A.
(2) When the output torque is 9 Nm, and the rotating speed is 3000 r/min, the iron loss can be suppressed by 12 W by giving the i_m of 6.6 A. In addition, the iron loss suppression effect increases as the rotating speed increases.

In chapter V, the prototype's efficiency was derived based on the loss formulation. Besides, the i_{om} was calculated by the result of the efficiency derivation. As a result, it was found that the i_{om} depends mainly on torque. Finally, the calculated and measured values of the efficiency were compared, and the validity of the formulation of loss and efficiency proposed in this paper was proved. In addition, it was revealed through the experiment that the efficiency in the high-torque driving range is improved by 2% to 4%, and the high-efficiency driving range can be expanded by using the i_{om}.

It has been revealed from the author's reference [14] that it is effective to use the square-wave zero-sequence current, which can be controlled by a three-phase four-wire inverter, as the i_m. However, when the zero-sequence current is used, it is necessary to consider additional losses, such as iron

loss caused during the square-wave zero-sequence current polarity switching. For the sake of simplification, this paper investigated the high-efficiency drive method of the prototype motor with the system that uses both the three-phase three-wire inverter and the DC power supply. Therefore, in future work, the high-efficiency drive method will be studied when the zero-sequence current is used as the i_m.

REFERENCES

[1] R. Tsunata, M. Takemoto, S. Ogasawara, and K. Orikawa, "Variable flux memory motor employing double-layer delta-type PM arrangement and large flux barrier for traction applications," *IEEE Trans. Ind. Appl.*, vol. 57, no. 4, pp. 3545–3561, Jul. 2021.
[2] K. Sakai, K. Yuki, Y. Hashiba, N. Takahashi, K. Yasui, and L. Kovudhikulrungsri, "Principle and basic characteristics of variable-magnetic-force memory motors," *IEEJ Trans. Ind. Appl.*, vol. 131, no. 1, pp. 53–60, 2011.
[3] J. Chen, J. Li, and R. Qu, "Maximum-torque-per-ampere and magnetization-state control of a variable-flux permanent magnet machine," *IEEE Trans. Ind. Electron.*, vol. 65, no. 2, pp. 1158–1169, Feb. 2018.
[4] X. Zhu, Z. Xiang, L. Quan, W. Wu, and Y. Du, "Multimode optimization design methodology for a flux-controllable stator permanent magnet memory motor considering driving cycles," *IEEE Trans. Ind. Electron.*, vol. 65, no. 7, pp. 5353–5366, Jul. 2018.
[5] Y.-H. Lee, M. F. Hsieh, and P.-H. Chen, "A novel variable flux spoke type permanent magnet motor with swiveling magnetization for electric vehicles," *IEEE Access*, vol. 10, pp. 62194–62209, 2022.
[6] A. Athavale, T. Fukushige, T. Kato, C.-Y. Yu, and R. D. Lorenz, "Variable leakage flux IPMSMs for reduced losses over a driving cycle while maintaining suitable attributes for high-frequency injection-based rotor position self-sensing," *IEEE Trans. Ind. Appl.*, vol. 52, no. 1, pp. 234–241, Jan. 2016.
[7] T. Kato, H. Hijikata, M. Minowa, K. Akatsu, and R. D. Lorenz, "Design methodology for variable leakage flux IPM for automobile traction drives," in *Proc. IEEE Energy Convers. Congr. Exposit. (ECCE)*, Sep. 2014, pp. 3548–3555.
[8] L. Xu, X. Zhu, W. Wu, W. Fan, X. Zhou, X. Cai, and L. Quan, "Flux-leakage design principle and multiple-operating conditions modeling of flux leakage controllable PM machine considering driving cycles," *IEEE Trans. Ind. Electron.*, vol. 69, no. 9, pp. 8862–8874, Sep. 2022.
[9] H. Hijikata, Y. Sakai, K. Akatsu, Y. Miyama, H. Arita, and A. Daikoku, "Wide speed range operation by low-voltage inverter-fed MATRIX motor for automobile traction motor," *IEEE Trans. Power Electron.*, vol. 33, no. 8, pp. 6887–6896, Aug. 2018.
[10] H. Hijikata, Y. Sakai, K. Akatsu, Y. Miyama, H. Arita, and A. Daikoku, "Multi-phase inverter-fed MATRIX motor for high efficiency driving," *IEEJ Trans. Ind. Appl.*, vol. 138, no. 3, pp. 257–264, 2018.
[11] J. A. Tapia, F. Leonardi, and T. A. Lipo, "Consequent-pole permanent-magnet machine with extended field-weakening capability," *IEEE Trans. Ind. Electron.*, vol. 39, no. 6, pp. 1704–1709, Nov./Dec. 2003.
[12] T. Mizuno, K. Nagayama, T. Ashikaga, and T. Kobayashi, "Basic principles and characteristics of hybrid excitation type synchronous machine," *IEEJ Trans. Ind. Appl.*, vol. 115, no. 11, pp. 1402–1411, 1995.
[13] K. Iwama and T. Noguchi, "Operation characteristics of adjustable field IPMSM utilizing magnetic saturation," *Energies*, vol. 15, no. 1, p. 52, Dec. 2021.
[14] K. Iwama and T. Noguchi, "Three-phase inverter fed adjustable field IPMSM drive utilizing zero-sequence current," *IEEE Trans. Ind. Electron.*, vol. 70, no. 2, pp. 1239–1249, Feb. 2023.
[15] T. Sun and J. Wang, "Extension of virtual-signal-injection-based MTPA control for interior permanent-magnet synchronous machine drives into the field-weakening region," *IEEE Trans. Ind. Electron.*, vol. 62, no. 11, pp. 6809–6817, Nov. 2015.
[16] X. Zhang, G. H. B. Foo, and M. F. Rahman, "A robust field-weakening approach for direct torque and flux controlled reluctance synchronous motors with extended constant power speed region," *IEEE Trans. Ind. Electron.*, vol. 67, no. 3, pp. 1813–1823, Mar. 2020.
[17] S. Y. Jung, C. C. Mi, and K. Nam, "Torque control of IPMSM in the field-weakening region with improved DC-link voltage utilization," *IEEE Trans. Ind. Electron.*, vol. 62, no. 6, pp. 3380–3387, Jun. 2015.
[18] S. Chaithongsuk, B. Nahid-Mobarakeh, J.-P. Caron, N. Takorabet, and F. Meibody-Tabar, "Optimal design of permanent magnet motors to improve field-weakening performances in variable speed drives," *IEEE Trans. Ind. Electron.*, vol. 59, no. 6, pp. 2484–2494, Jun. 2012.
[19] J. Liu, C. Gong, Z. Han, and H. Yu, "IPMSM model predictive control in flux-weakening operation using an improved algorithm," *IEEE Trans. Ind. Electron.*, vol. 65, no. 12, pp. 9378–9387, Dec. 2018.
[20] Q. Guo, C. Zhang, L. Li, J. Zhang, and M. Wang, "Maximum efficiency per torque control of permanent-magnet synchronous machines," *IEEE Trans. Ind. Electron.*, vol. 6, no. 12, pp. 2135–2143, Dec. 2016.
[21] G. Bertotti, "General properties of power losses in soft ferromagnetic materials," *IEEE Trans. Magn.*, vol. MAG-24, no. 1, pp. 621–630, Jan. 1988.
[22] Z. Huang, J. Fang, X. Liu, and B. Han, "Loss calculation and thermal analysis of rotors supported by active magnetic bearings for high-speed permanent-magnet electrical machines," *IEEE Trans. Ind. Electron.*, vol. 63, no. 4, pp. 2027–2035, Apr. 2016.
[23] P. H. Mellor, R. Wrobel, and D. Holliday, "A computationally efficient iron loss model for brushless AC machines that caters for rated flux and field weakened operation," in *Proc. IEEE Int. Electric Mach. Drives Conf.*, May 2009, pp. 490–494.

KIYOHIRO IWAMA (Graduate Student Member, IEEE) was born in Fuji, Japan, in 1995. He received the B.Eng. and M.Eng. degrees from Shizuoka University, Hamamatsu, Japan, in 2018 and 2020, respectively, where he is currently pursuing the Ph.D. degree with the Department of Environment and Energy System, Graduate School of Science and Technology.

His research subject since, he was an undergraduate has been motor hardware of an adjustable field PMSM and its drive systems.

Mr. Iwama is a Student Member of the Institute of Electrical Engineers of Japan (IEEJ).

TOSHIHIKO NOGUCHI (Senior Member, IEEE) was born in Kuwana, Japan, in 1959. He received the B.Eng. degree in electrical engineering from the Nagoya Institute of Technology, Nagoya, Japan, in 1982, and the M.Eng. and D.Eng. degrees in electrical and electronics systems engineering from the Nagaoka University of Technology, Nagaoka, Japan, in 1986 and 1996, respectively.

In 1982, he was with Toshiba Corporation, Tokyo, Japan. He was a Lecturer with the Gifu National College of Technology, Gifu, Japan, from 1991 to 1993. He was an Assistant Professor and an Associate Professor with the Department of Electrical, Electronics and Information Engineering, Nagaoka University of Technology, from 1994 to 1995 and from 1995 to 2009, respectively. Since 2009, he has been a Professor with the Department of Electrical and Electronics Engineering, Faculty of Engineering, Graduate School of Engineering, Shizuoka University, Hamamatsu, Japan. His research interests include new circuit topologies of static power converters and motor drives including electric machine hardware.

Mr. Noguchi is a member of the Institute of Electrical Engineers of Japan.